JACS
JOURNAL OF THE AMERICAN CHEMICAL SOCIETY
pubs.acs.org/JACS
Article

Real-Time Detection of Hydroxyl Radical Generated at Operating Electrodes via Redox-Active Adduct Formation Using Scanning Electrochemical Microscopy

Jaxiry S. Barroso-Martínez,[§] Adolfo I. B. Romo,[§] Sanja Pudar, Seth T. Putnam, Erika Bustos, and Joaquín Rodríguez-López*

Cite This: J. Am. Chem. Soc. 2022, 144, 18896−18907
Read Online
ACCESS | Metrics & More | Article Recommendations | Supporting Information

ABSTRACT: The hydroxyl radical (•OH) is one of the most attractive reactive oxygen species due to its high oxidation power and its clean (photo)(electro)generation from water, leaving no residues and creating new prospects for efficient wastewater treatment and electrosynthesis. Unfortunately, in situ detection of •OH is challenging due to its short lifetime (few ns). Using lifetime-extending spin traps, such as 5,5-dimethyl-1-pyrroline *N*-oxide (DMPO) to generate the [DMPO−OH]• adduct in combination with electron spin resonance (ESR), allows unambiguous determination of its presence in solution. However, this method is cumbersome and lacks the necessary sensitivity and versatility to explore and quantify •OH generation dynamics at electrode surfaces in real time. Here, we identify that [DMPO−OH]• is redox-active with E^0 = 0.85 V vs Ag|AgCl and can be conveniently detected on Au and C ultramicroelectrodes. Using scanning electrochemical microscopy (SECM), a four-electrode technique capable of collecting the freshly generated [DMPO−OH]• from near the electrode surface, we detected its generation in real time from operating electrodes. We also generated images of [DMPO−OH]• production and estimated and compared its generation efficiency at various electrodes (boron-doped diamond, tin oxide, titanium foil, glassy carbon, platinum, and lead oxide). Density functional calculations, ESR measurements, and bulk calibration using the Fenton reaction helped us unambiguously identify [DMPO−OH]• as the source of redox activity. We hope these findings will encourage the rapid, inexpensive, and quantitative detection of •OH for conducting informed explorations of its role in mediated oxidation processes at electrode surfaces for energy, environmental, and synthetic applications.

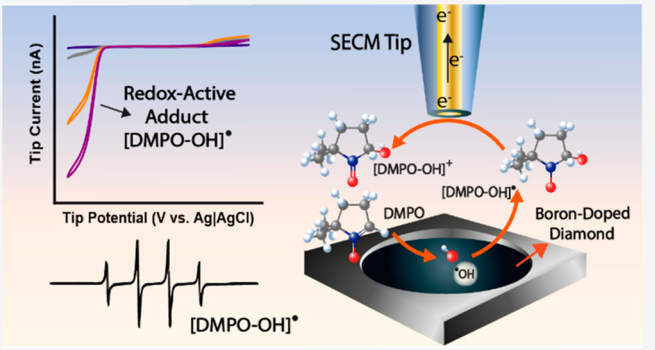

1. INTRODUCTION

Among the reactive oxygen species (ROS), the hydroxyl radical (•OH) emerges as a key intermediate for "clean oxidations" due to its high positive redox potential (2.73 V vs RHE),[1−3] its swift generation from water or oxygen, and its ability to oxidize species in aqueous solutions without leaving residues.[4−7] The generation of •OH at electrode surfaces is of particular interest due to its dynamic control and potential for incorporating renewable electrical energy for producing it in environmental and synthetic applications. A broad variety of applications including advanced oxidation processes (AOPs) for wastewater treatment, photoelectrochemical processes, and even cancer therapies have benefited from its generation at electrodes.[8−18] Prospects exist for the large-scale applications of AOPs for removing organic pollutants from rivers and tributaries through their mineralization to CO_2.[19−22] Despite its importance and its common involvement in proposed reaction mechanisms for electrooxidations, direct evidence of electrogenerated •OH is not often presented. The pioneering work of Comninellis and others using spin-traps[23,24] demonstrated that •OH is indeed produced at electrochemical surfaces such as boron-doped diamond (BDD). However, the generation of •OH at electrodes produces small amounts of the radical, significantly complicating its quantification and often requiring long electrolysis experiments using indirect assays, which often last several minutes to hours. This makes it difficult to discern •OH participation in competing pathways involving other ROS and in processes involving direct electrochemical oxidation at the electrode surface.

The hydroxyl radical is typically generated in a controllable fashion via two different methods: (i) by Fenton-like reactions[25,26] and (ii) at electrochemical/photoelectrochemical

Received: June 14, 2022
Published: October 10, 2022

interfaces.[27−29] Fenton-like reactions are based on the oxidation of a metallic ion or metal complex in the presence of hydrogen peroxide. The most widely used metal for Fenton chemistry is iron. In this method, H_2O_2 reduction by Fe^{II} produces Fe^{III} and •OH, as shown in eq 1. On the other hand, the (photo)electrochemical process proceeds through the one-electron oxidation of water to generate •OH, as shown in eq 2. Here, the most widely used electrode materials are boron-doped diamond (BDD)[30−34] or titanium oxide nanocrystals.[10,28,35−37] On electrochemical systems such as BDD, •OH generation is in competition with other pathways to oxidize water, such as the four-electron process to generate O_2.

$$Fe(II) + H_2O_2 \rightarrow Fe(III) + OH^- + {}^{\cdot}OH \quad (1)$$

$$(Surface)-OH_2 \rightarrow e^- + H^+ + {}^{\cdot}OH \quad (2)$$

Due to its extreme reactivity and short lifetime (~1 ns),[38] •OH detection is quite challenging on heterogeneous systems. However, detection in homogeneous phase, as it occurs during generation using the Fenton process, is conveniently performed using spin traps. The resulting adduct is then analyzed via electron spin resonance (ESR).[39−41] A common method involves the addition of a fast-reacting spin trap such as 5,5-dimethyl-1-pyrroline *N*-oxide (DMPO) to form the [DMPO−OH]• adduct, eq 3. In contrast to the fleeting •OH intermediate, this adduct has a longer lifetime of minutes to hours.[42]

$$DMPO + {}^{\cdot}OH \rightarrow [DMPO-OH]^{\cdot} \quad (3)$$

ESR measurements unequivocally identify the formation of [DMPO−OH]• because it can be fingerprinted through its hyperfine coupling.[42,43] Thus, ESR brings mechanistic value in distinguishing •OH formation from that of other ROS, which may also be formed. ESR can also be used to determine the concentration of spins trapped in the solution.[44] However, ESR has several drawbacks: the sensitivity of the technique unless an optimized setup is used, as the typical sensitivity of the technique is of the order of micromolar and, therefore, sets a limit on the minimum number of detectable species in a bulk solution volume. This may not be a particular issue with the Fenton process performed in homogeneous phase. However, it creates a critical constraint on studies at electrodes, because these typically produce a limited amount of •OH in the vicinity of the electrode.[45] Thus, only electrolysis for long periods of time (several minutes to hours)[23,24] generates a detectable concentration. This hampers the real-time detection of •OH and the elucidation of its formation dynamics and interactions with other species at the electrode. Identifying electrode materials and conditions that selectively produce •OH in high yield and characterizing its reactions with solution species (e.g., pollutants) is critical to advancing technologies such as AOPs. Therefore, it is pressing to develop an approach for measuring •OH generation at electrodes at the shortest time scale possible.

Here, we directly tackle the issue of low sensitivity in ESR studies at electrodes by demonstrating that the [DMPO−OH]• adduct is redox-active and, thus, can be detected in situ with high sensitivity within the diffusion layer of the electrode. To do so efficiently, we used scanning electrochemical microscopy (SECM) in the substrate generation/tip collection mode (SG/TC). In short, and as depicted in Scheme 1, an ultramicroelectrode (UME) probe positioned in the vicinity of an operating electrode was biased to electrolyze the [DMPO−OH]• generated locally as a result of eq 3. By comparing our electrochemical measurements to DFT predictions of redox potential for [DMPO−OH]•, and using ESR signatures from solution near the electrode surface, we unambiguously identified this species. We show the versatility of our method by obtaining comparative generation efficiencies of [DMPO−OH]• on several electrode surfaces and by imaging its production on an operating BDD electrode.

Scheme 1. Use of Scanning Electrochemical Microscopy (SECM) To Collect the [DMPO−OH]• Adduct Formed from Spin Trapping of •OH Radicals Generated on Boron-Doped Diamond Electrodes at Different Applied Potentials (E_{BDD}) Using Cyclic Voltammetry at the SECM Tip

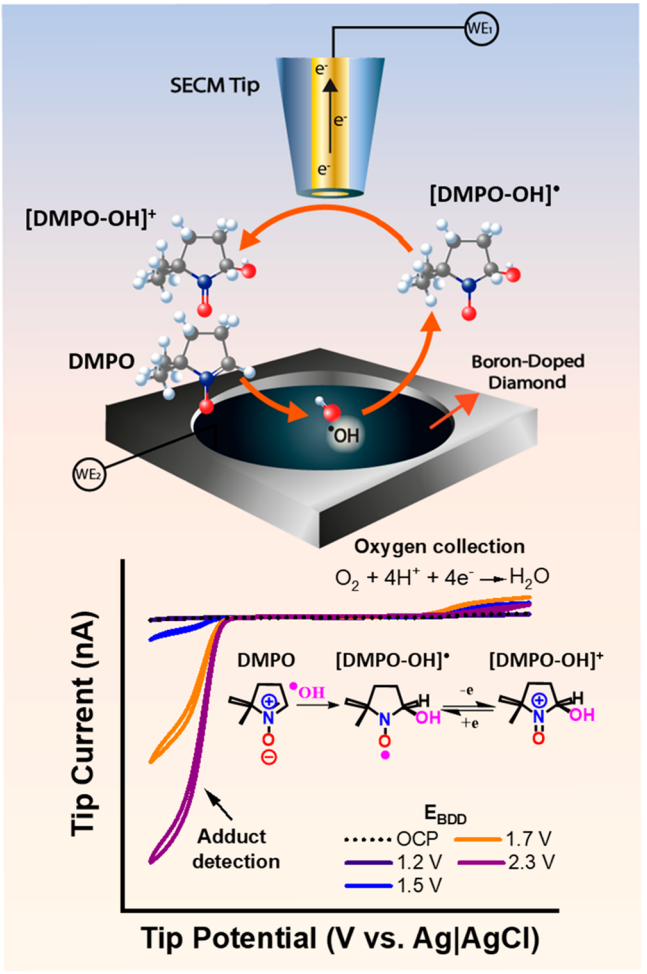

2. RESULTS AND DISCUSSION

2.1. Detection of a Redox-Active Adduct. We first characterized the redox activity of the [DMPO−OH]• adduct. SG/TC experiments were performed by approaching a 12.5 μm radius gold UME as the SECM tip to a BDD electrode and positioning it 10 μm away from the surface (Figure S1). We carried out SECM tip cyclic voltammetry (CV) experiments at 10 mV s^{-1} designed to resolve the tip potential at which species were collected as a function of the potential of the BDD electrode. These experiments were performed in 0.1 M Na_2SO_4 at pH 4, with and without DMPO in solution. Figure 1a shows a current signal at the SECM tip in two different potential regions. We ascribe the collection process observed at the more negative potentials (~0 vs Ag|AgCl) to oxygen

https://doi.org/10.1021/jacs.2c06278
J. Am. Chem. Soc. 2022, 144, 18896−18907

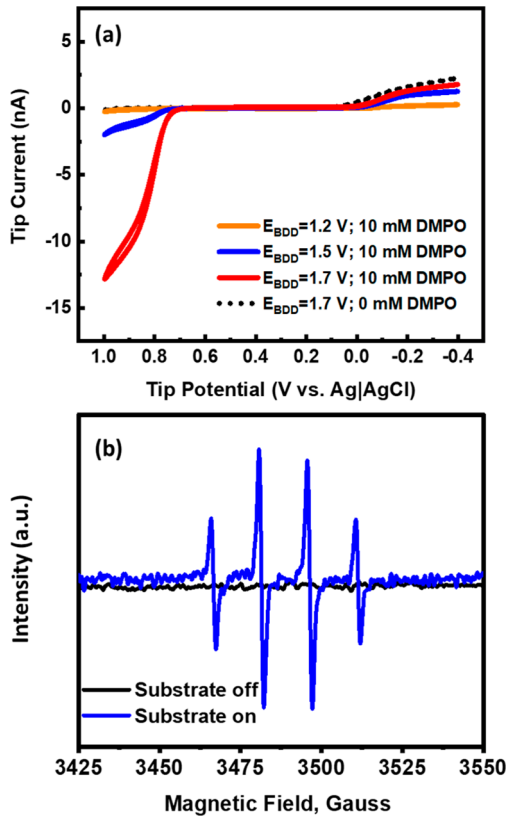

Figure 1. (a) Collection experiments on gold SECM tip by applying different potentials on the BDD electrode immersed in 0.1 M Na_2SO_4 at pH 4 in the absence and presence of 10 mM DMPO, and (b) ESR spectra of a solution containing 10 mM of DMPO and 0.1 M of Na_2SO_4 pH 4 sampled from near the surface of BDD electrode when it was turned on (E_{BDD} = 1.7 V vs Ag|AgCl) and off. Hyperfine coupling parameters α^N = 14.9 G and α_β^H = 14.89 G.

evolution from the BDD, consistent with the detection of oxygen in a bulk solution under the same conditions. On the other hand, the well-defined wave with $E_{1/2}$ = 0.85 V was only observed in the presence of DMPO. The intensity of the signal was also dependent on the applied potential on the BDD electrode, E_{BDD}. To understand the behavior of this redox process, we first identified the species responsible.

2.2. DFT and ESR Characterization of Adducts. We resorted to density functional theory (DFT) methods to predict the redox potential of possible adducts of DMPO formed upon reaction with •OH. [DMPO−OH]• is structurally depicted in Scheme 2 along with other possible products and their corresponding redox reactions.

It has been reported that species such as [DMPO−OH]• decay to [DMPO═O]•, while [DMPO−OOH]• species decay to [DMPO−OH]•.[44,46] We selected four methods to predict the redox potential of DMPO−X species (Table S1), including the solvation model based on density (SMD) and polarizable continuum model (PCM) solvation using the Born−Haber cycle, along with corrections for SHE potentials. Averaging the predictions from these methods, we found reversible redox reactions for [DMPO−OH]• at 0.77 ± 0.06 V vs Ag|AgCl, for [DMPO−OOH]• at 0.92 ± 0.04 V vs Ag|AgCl, and for [DMPO═O]• at 1.55 ± 0.04 V vs Ag/AgCl. Clearly, the experimental $E_{1/2}$ of 0.85 V vs Ag|AgCl allows us to rule out [DMPO═O]•. Within error, both [DMPO−OH]• and [DMPO-OOH]• are plausible species. To decide between

Scheme 2. Representation of [DMPO−OH]• (Top), [DMPO−OOH]• (Middle), and [DMPO═O]• (Bottom) Adducts and Their Reversible Redox Reactions

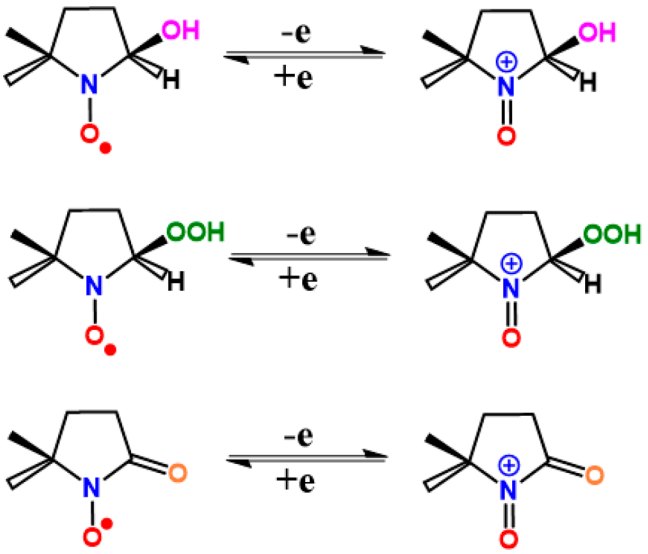

these two as the source of redox reactivity, we carried out ESR experiments.

We electrolyzed a 0.1 M Na_2SO_4 solution at pH 4 using a BDD electrode. Aliquots sampled from the vicinity of the electrode using a fine-tip Hamilton syringe were taken before and after applying a potential of 1.6 V on the substrate (Figure 1b). No paramagnetic signal was observed when the substrate was at open circuit. However, the characteristic hyperfine couplings for the [DMPO−OH]• adduct were observed when the substrate was on. The 1:2:2:1 integration ratio of the hyperfine signals, together with the values of α^N = 14.9 G and α_β^H = 14.89 G, unequivocally prove that the species generated by the BDD substrate is [DMPO−OH]• (Figure 1b). This indicates the straightforward adduct-formation reaction between •OH and DMPO in eq 3.[39−41] Experiments at variable pH (Figure S2) showed that the formation of the [DMPO−OH]• is also observed at more acidic pH values. In contrast, the formation of the [DMPO═O]• species was observed at pH 7. This adduct has 9 characteristic hyperfine coupling signals and values of α^N = 7.26 G and α_β^H = 4.03 G.[47] Additionally, we observed that, at pH 4 and pH 1 after 20 min of starting the reaction, [DMPO−OH]• began to decay generating [DMPO═O]• (Figure S3). Altogether, DFT and ESR experiments strongly suggest that the predominantly formed species at the BDD surface is [DMPO−OH]•. We believe that this species is also formed at pH 7, but the time scale of the experiment and ESR measurement (∼2 min) prevent us from observing it directly, instead only detecting the decay product. This fact reinforces the importance of evaluating this species with an in situ generation and quantification method. Assuming that the diffusion coefficient (D) for [DMPO−OH]• is 1×10^{-9} m^2 s^{-1} and solving for the diffusional time $t = d^2/2D$ in our SECM setup, with d = 10 μm as the interelectrode distance, the time it takes from generation to detection of [DMPO−OH]• is t = 50 ms, swiftly outpacing the decay of the adduct.

2.3. Redox Behavior of [DMPO−OH]•. We now turn to understanding the characteristics of the anodic process resulting from the oxidation of [DMPO−OH]•. In the absence

https://doi.org/10.1021/jacs.2c06278
J. Am. Chem. Soc. 2022, 144, 18896−18907

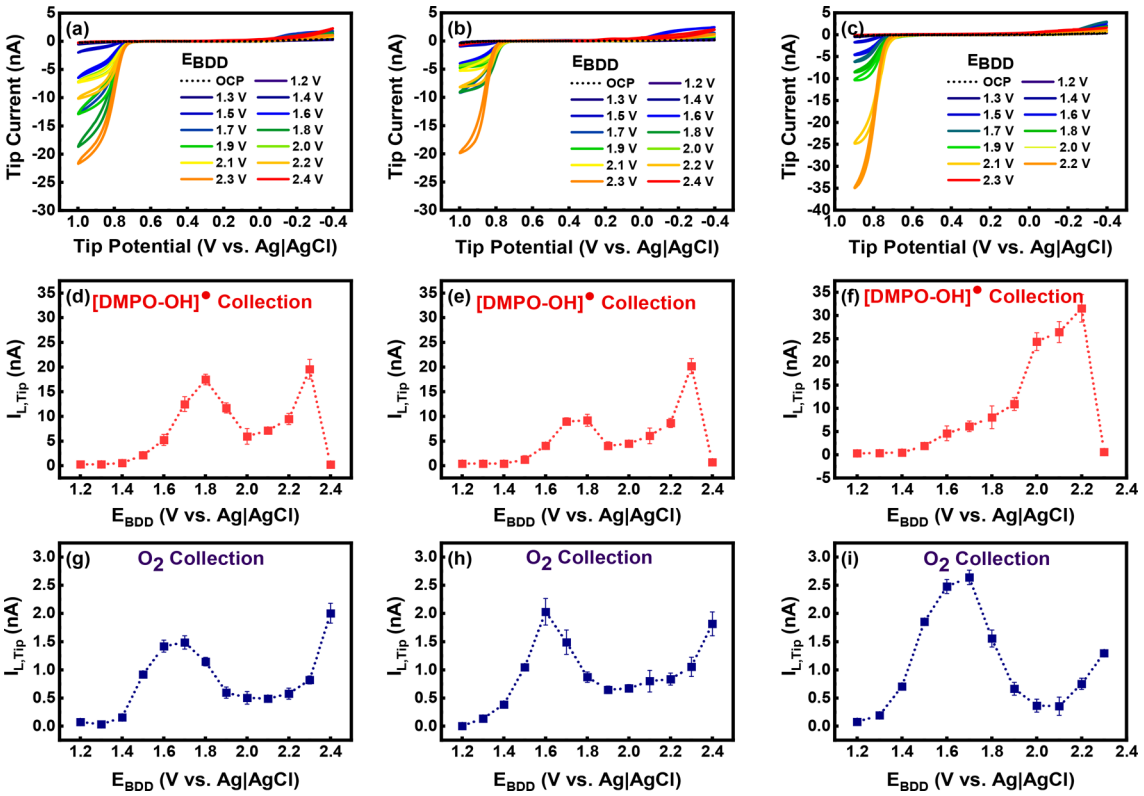

Figure 2. Collection experiments of the [DMPO−OH]• adduct (highlighted with orange) and O_2 evolution (highlighted with blue) from the BDD surface in Na_2SO_4 pH 4 (left column), Na_2SO_4 pH 7 (middle column), and PB pH 7.4 (right column). Orange plots in second row correspond to [DMPO−OH]• collection current while blue plots in third row correspond to O_2 collection current, all as a function of the substrate potential during the CVs in the figures on first row.

of DMPO in solution, the redox wave at ∼0.85 V vs Ag|AgCl was not observed. Similarly, addition of DMPO to solution (tested between 0.1 mM up to 50 mM) did not show any redox wave on the SECM tip until the substrate was biased to a critical BDD potential (see below). Furthermore, distance dependence of the SECM tip response as it was pulled away from the BDD substrate clearly showed a lower signal (Figure S4), as expected for a decreasing SG/TC SECM signal at greater tip−substrate distance.[48] However, we also note that, at the BDD substrate potentials used here, we would expect that oxidation of [DMPO−OH]• at the substrate would produce a reducible species in during collection experiments. We believe the oxidized form self-discharges in solution to generate the reduced form of the $[DMPO-OH]^{+/\bullet}$ redox pair within the diffusional time span of the collection process. In fact, in SECM experiments at very short distance, which in SECM translates to a shorter diffusional time (Figure S4), we do observe a cathodic component to the [DMPO−OH]• wave, consistent with this proposition. Given these observations, we cannot discard that the discharge process or the oxidation of [DMPO−OH]• at the surface of the substrate electrode could lower the collected amount at the tip. DMPO could interact with BDD or other substrates in various fashions, so we cannot fully discard that either heterogeneous or homogeneous phase interactions affect our measurements. However, given similar experimental conditions, we believe that all comparisons in the behavior of different materials in subsequent sections remain valid.

These results highlight the critical role of a four-electrode measurement, where the collector SECM tip is capable of detecting the [DMPO−OH]• adduct based on its own redox potential, and not through a process that is convolved with the reactivity of the BDD electrode as otherwise occurs in a three-electrode setup.[49] It is also noteworthy that the measured response is not due to the formation of hydrogen peroxide from the BDD electrode (Figure S5), which is consistent with our previous reports of water oxidation and the detection of adsorbed ROS at BDD.[50] We also noticed that the process is independent of the material used for the construction of the SECM tip, as we were able to detect the redox wave at both Au and C (Figure S6). This suggests the redox process is outer-sphere, consistent with the straightforward 1e process depicted in Scheme 2.[51] We note that on C fiber electrodes, the redox wave is less well-defined in comparison to Au. In turn, it is important to limit the potential window of Au to less than 1 V vs Ag|AgCl, to avoid interference from surface gold oxides which form at potentials close from the redox wave. As expected from a bimolecular adduct formation process, we observed that the intensity of the oxidation wave is dependent on the concentration of DMPO (Figure S7a). A saturation point (Figure S7b) is reached at sufficiently high concentrations of DMPO (∼50 mM). Finally, Scheme 2 suggests that the predicted redox reaction involving the oxidation of [DMPO−OH]• should be pH-independent. This was experimentally verified by comparing the redox wave observed at pH 4, and pH 7 and pH 7.4 upon activation of the BDD electrode (Figure S8).

With knowledge on the properties of the [DMPO−OH]• redox wave detected at the SECM tip, we can now focus on the behavior exhibited by BDD as the potential and pH is changed.

https://doi.org/10.1021/jacs.2c06278
J. Am. Chem. Soc. 2022, 144, 18896−18907

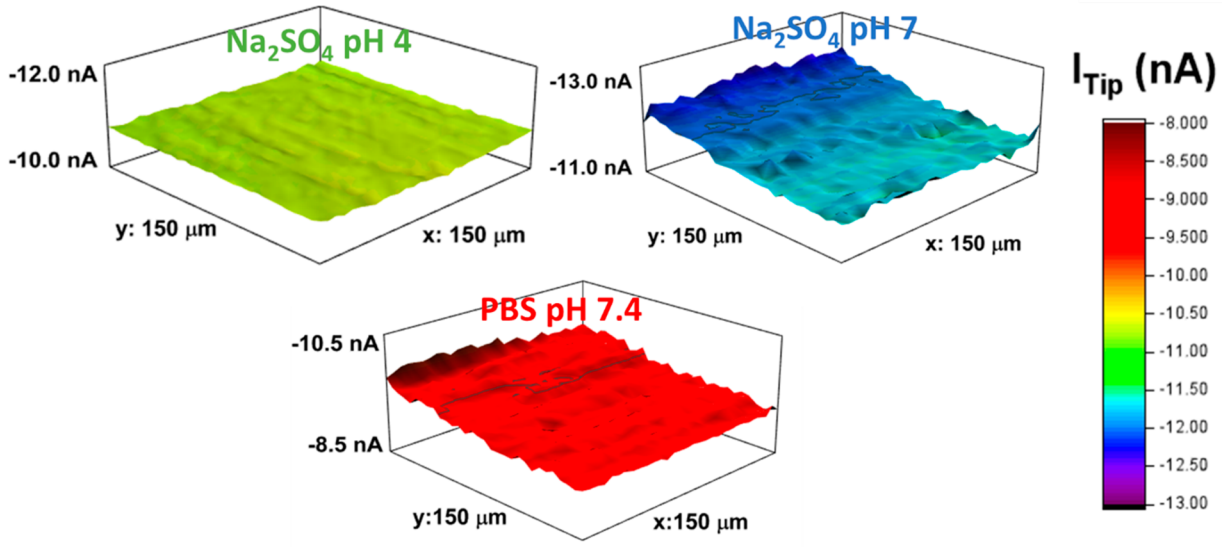

Figure 3. SECM images on BDD at E_{BDD} = 1.8 V vs AgIAgCl for [DMPO−OH]• collections in Na_2SO_4 pH 4, Na_2SO_4 pH 7, and PBS pH 7.4.

The first row of Figure 2 displays [DMPO−OH]• collection experiments in 0.1 M Na_2SO_4 acidified to pH 4 using H_2SO_4, 0.1 M Na_2SO_4 at pH 7 and 0.1 M phosphate buffer solution (PBS) adjusted to pH 7.4, respectively. In these graphs the SECM tip limiting current ($I_{L,Tip}$) clearly changes as a function of the potential applied to BDD. These trends are more clearly shown in the middle section of Figure 2. These plots allow us to appreciate that [DMPO−OH]• collection starts at ∼1.4 V vs AgIAgCl. Eventually $I_{L,Tip}$ increases until E_{BDD} reaches 2.4 V vs AgIAgCl at Na_2SO_4 pH 4 and pH 7, and 2.5 V vs AgIAgCl at PBS pH 7.4. At these potentials, the anodic wave on the SECM tip disappears. We hypothesize that at these E_{BDD} potentials, DMPO becomes unviable, possibly due to its electrolysis at the electrode surface. Alternatively, •OH generation may be ceasing. To explore this change in output, we polarized the SECM tip to more negative potentials during CV, which allowed us to probe O_2 evolution from the BDD electrode by using the oxygen reduction reaction at the tip. A strong dependency for O_2 collection, produced via the 4e water oxidation on BDD, is shown in the third row of Figure 2. This oxygen collection signal starts to appear also when BDD is biased at 1.4 V vs AgIAgCl. $I_{L,Tip}$ at all pH conditions shows that the O_2 signal increases concomitantly with a signal decrease of the [DMPO−OH]• anodic wave. Thus, the observed dependence strongly suggests a competition between the 1e water oxidation pathway to form •OH,[23] and the 4e pathway to form O_2 at the BDD electrode. SECM collection experiments allowed to probe these competing processes with within the same measurement, highlighting their versatility.

We further took advantage of the imaging capabilities of SECM as the tip was rastered at constant distance from the substrate to spatially resolve [DMPO−OH]• formation. We biased the SECM tip to 0.9 V vs AgIAgCl to obtain SECM images in the SG/TC mode, where the probe continuously collected [DMPO−OH]• as the BDD electrode generated •OH at constant E_{BDD}. Figure 3 shows that regardless of the pH used, the tip response is fairly homogeneous over a domain of hundreds of microns in size, even if the rate of production rate of [DMPO−OH]• was different at each pH. Each map was obtained around the same probed area. These results indicate that the point measurements performed in Figure 2 are representative of the whole BDD electrode surface. Overall, the SECM toolset introduced here is capable not only of estimating the real-time generation of •OH at an electrode, but also of providing mapping capabilities that might be useful in the inspection of more heterogeneous interfaces than BDD.

2.4. Comparative Generation Efficiency of [DMPO−OH]• at Different Electrode Surfaces. A primary advantage of our electrochemical method to detect [DMPO−OH]• as a proxy for •OH generation is its ability to estimate its instantaneous rate of generation. With this in mind, we carried out finite element method simulations (Figure S9) to calibrate the SECM response and evaluate •OH flux from the observed limiting current at the tip. This quantitative relationship is shown in Figure S9b for the geometry used here, displaying a linear relationship between the tip current and the simulated generation rate of •OH at the electrode. Knowing that the generation of [DMPO−OH]• is homogeneous on the BDD surface (Figure 3), with the estimated generation rates as described above, and with the experimental substrate current, we can determine a generation efficiency for [DMPO−OH]• at each condition and electrode surface (see Experimental Section 4.8).

Figure S10 shows the experimental [DMPO−OH]• collection as a function of potential for different materials, including BDD, fluorine-doped tin oxide (FTO), lead oxide (PbO_2|Pb), titanium foil (Ti), platinum (Pt), and glassy carbon (GC). In addition, Figure S11 shows the corresponding substrate currents at the moment of [DMPO−OH]• collection in Figure S10. Many of these electrodes have been described as •OH-generating materials.[52] In general, [DMPO−OH]• generation efficiencies for BDD in Figure 4a show similar trends to the limiting currents shown in Figure 2. From 1.3 to 1.4 V vs AgIAgCl in BDD, efficiencies between 1% and 2% begin to be registered. As the potential of the BDD increases, efficiency increases until it reaches maximum values of ∼5% between 1.8 and 2.2 V vs AgIAgCl, before declining to 0% when [DMPO−OH]• collection drops as described in the

https://doi.org/10.1021/jacs.2c06278
J. Am. Chem. Soc. 2022, 144, 18896−18907

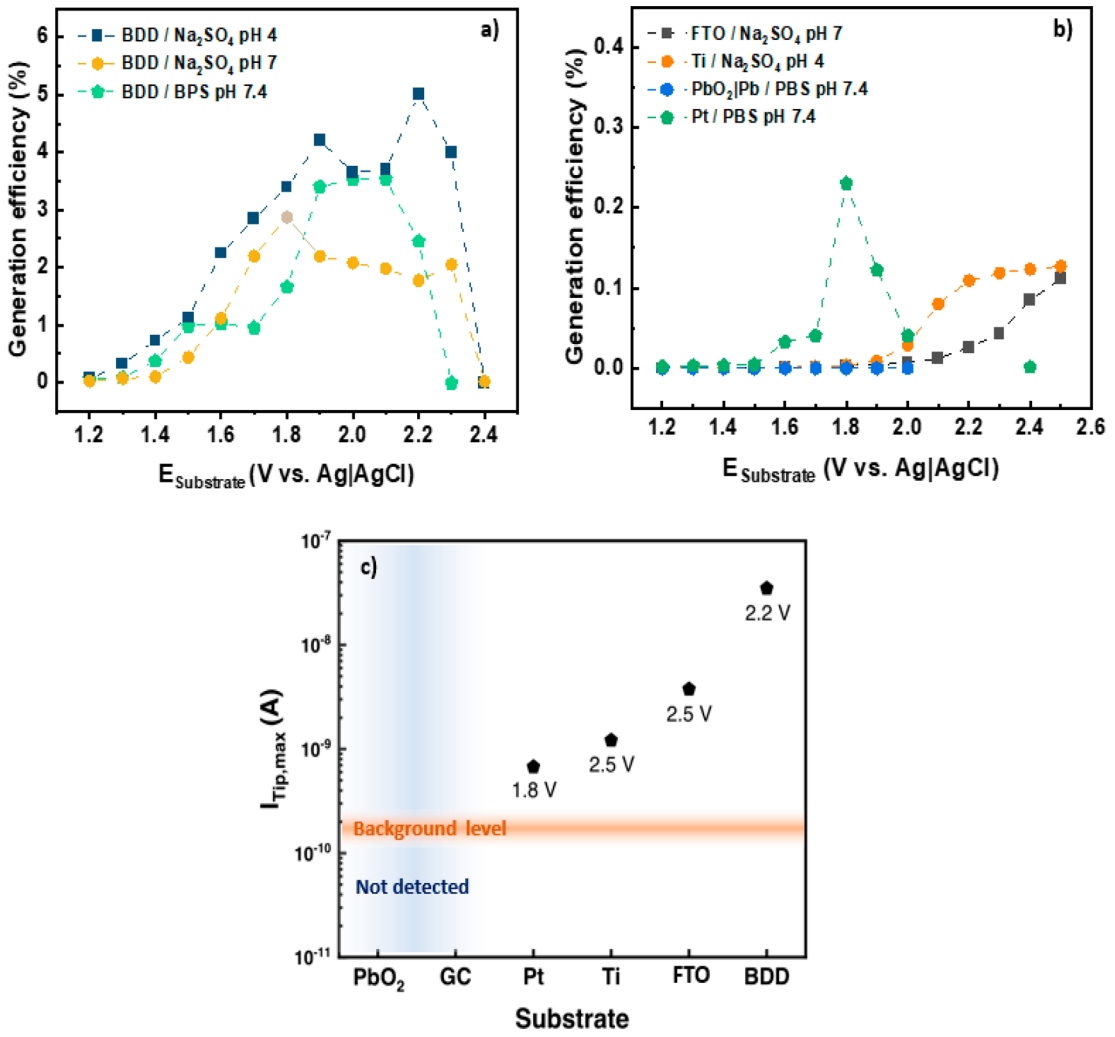

Figure 4. Estimated generation efficiencies from COMSOL Multiphysics-aided model for formation of $[DMPO{-}OH]^{\bullet}$ at different potentials of electrolysis on (a) BDD substrate at different pH condition. Light blue zone shows area of uncertainty where $[DMPO{-}OH]^{\bullet}$ collection sharply declines. (b) Generation efficiency at different substrates used for $[DMPO{-}OH]^{\bullet}$ adduct generation. (c) Comparative plot of substrate vs $I_{tip,max}$, the highest collection current observed experimentally with the potential at which it occurred indicated in the label. Notice $I_{tip,max}$ is in logarithmic scale. Maximum current observed in the Tip for the substrate were BDD = $(33.55 \times 10^{-9}) \pm (2.96 \times 10^{-9})$ A, FTO = $(3.75 \times 10^{-9}) \pm (0.75 \times 10^{-9})$ A and Ti = $(1.21 \times 10^{-9}) \pm (0.18 \times 10^{-9})$ A.

previous section. We speculate that differences in the generation efficiency of BDD at different pH are due to the competition of oxygen evolution, ionic strength effects at the interface, and the availability of H^+ and OH^-.[50] To this point, the highest efficiency evaluated was observed in acid medium, which is consistent with reports of $^{\bullet}OH$ generation being favored at lower pH.[53,54] In contrast to BDD, $[DMPO{-}OH]^{\bullet}$ generation is greatly decreased when using other samples, to the point that Figure 4b shows these results on a different vertical axis scale. Here, $[DMPO{-}OH]^{\bullet}$ generation at Pt shows a sharp rise and decline, with a peak at ~1.8 V vs Ag|AgCl. On FTO and Ti, collections are initially observed when they are polarized at 1.9 V vs Ag|AgCl, but then, as $E_{substrate}$ increases, the generation efficiency peaks around ~0.1% on these samples at 2.5 V vs Ag|AgCl. In the case of PbO_2|Pb and GC samples, no current associated with $[DMPO{-}OH]^{\bullet}$ production was observed. While $^{\bullet}OH$ has been proposed on other PbO_2 samples, our measurements beyond 2.0 V vs Ag|AgCl also became too unstable, possibly due to copious O_2 evolution. An important observation across different electrode materials that show activity is the great differences in both the potential and limiting current for maximum $[DMPO{-}OH]^{\bullet}$ generation, as shown in Figure 4c. We plot this maximum in a logarithmic scale at the observed potential. Figure 4c makes evident the inner-sphere, electrocatalytic nature of $^{\bullet}OH$ generation. It also provides an absolute measure of which materials produce more of this ROS. Overall, these observations confirm what has been inferred from other experiments in the literature: that BDD is the most efficient material for $^{\bullet}OH$ generation. Unlike those studies, here we provide a methodology to comparatively estimate this ROS in real time over a wider range of conditions and electrode potentials.

Assessing the various responses observed in Figure 4 raises the question about the electrode potential at which $^{\bullet}OH$ is formed, and its relation to the electrode material. On BDD, we observed its generation at potentials significantly lower than the standard potential of 2.73 V vs RHE. Taking as an example BDD in Na_2SO_4 pH 7, in our SECM collection experiments we observe peaking responses for $[DMPO{-}OH]^{\bullet}$ between 1.8 to 2.0 V vs Ag|AgCl and of 1.7 V vs Ag|AgCl for the peak in the CV response at the substrate (Figure S11). When a correction

https://doi.org/10.1021/jacs.2c06278
J. Am. Chem. Soc. 2022, 144, 18896−18907

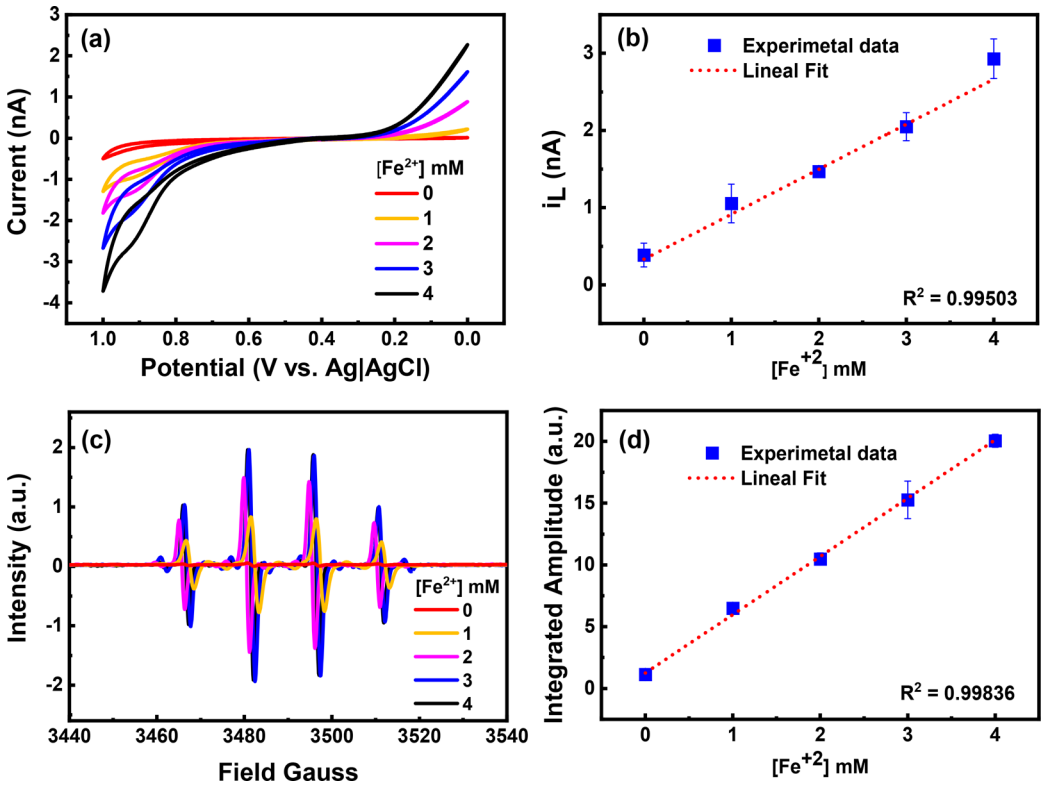

Figure 5. Performance comparison between electrochemical and ESR detection of [DMPO−OH]•. (a) Cyclic voltammetry of aqueous solution containing 100 mM of DMPO, various Fe^{2+} concentrations and 10 mM of H_2O_2. Gold UME (12.5 μm in radius) was used as working electrode, Pt and AglAgCl were used as counter and reference electrode respectively. (b) Plot of absolute limiting current vs Fe^{2+} concentration. (c) ESR spectrum of aqueous solution containing 100 mM of DMPO, various Fe^{2+} concentrations and 10 mM of H_2O_2. (d) Plot of integrated signals for [DMPO−OH]• adduct vs Fe^{2+} concentration. All results shown here were acquired after 2 min of reaction.

factor of 0.635 V is applied to account for pH and reference electrode differences, these peaks correspond to ∼2.435 to 2.635 V vs RHE and of 2.335 vs RHE, respectively. All these are below the nominal 2.73 V vs RHE. We reason that these differences are consistent with the adsorptive stabilization of •OH at the electrode surface, although to the best of our knowledge this has not been reported previously. Such underpotential adsorbed intermediates, e.g. adsorbed H or adsorbed O, are common in electrocatalytic processes such as in the hydrogen or water oxidation reactions.[55] In fact, previous measurements of our group using Surface Interrogation SECM with hydroxymethylferrocene (FcMeOH) as a redox mediator to titrate surface adsorbed ROS at BDD in Na_2SO_4 electrolyte at pH 7 detected an ROS consistent with the potentials reported here, with a peak response at ∼2.3 V vs RHE.[50]

Quaino and Schmickler[56] have recently reported computational studies of •OH at the BDD surface, concluding that the structure, oxygen coverage, type of termination, and environment all affect the adsorption of •OH at this surface. For instance, an "ether" configuration leads to a strongly bound •OH state while a "keto" configuration leads to a loosely bound one. The keto configuration was then found to proceed to an outer-sphere like oxidation of OH^- to ·OH in this study. This complexity in the BDD reaction pathways is not in conflict with the view of •OH as both a loosely bound species posed by Kapalka et al.[57] and potentially a stronger bound, yet reactive, state as suggested here. We notice that the highly defective BDD surface with nanocrystalline structure and presence of graphitic domains[34] used here may in fact prompt alternative mechanisms for water oxidation to generate •OH which then reacts with DMPO. While it is difficult to make direct comparisons to other works in the literature due to the lack of systematic structure−activity studies for •OH formation on BDD with reported characterization features, the methodology presented here creates the opportunity to do so in a variety of surfaces, and we expect to undertake these type of studies in the near future.

2.5. Correlation of [DMPO−OH]• Detection at UMEs to ESR. To further confirm the quantitative detection of [DMPO−OH]• using electrochemistry, we compared the responses observed with a UME to those obtained using ESR by probing a bulk solution where •OH was generated using well-established methods. We chose the Fenton reaction for the in situ generation of the [DMPO−OH]• adduct under similar conditions for electrochemical and ESR analysis. We first confirmed the redox stability of the Au SECM tip before and after contact with the Fenton reaction solution (Figure S12), where negligible changes were observed on the FcMeOH redox. We used DMPO as spin trap for the reaction of Fe^{2+} with H_2O_2 to conduct the formation of •OH. The limiting current for the [DMPO−OH]• signal was followed for different Fenton reagent concentrations by CV, as shown in Figure 5a. We plotted $I_{L,Tip}$ at each different Fe^{2+} concentration and obtained a linear trend with correlation coefficient R^2 = 0.99503, Figure 5b. ESR measurements showed hyperfine coupling values of α^N = 14.89 G and α_β^H = 14.88 G, consistent with [DMPO−OH]• formation, Figure 5c. We obtained a calibration curve based on the spins determined by ESR. The paramagnetic signals were integrated, and the area in the curve

https://doi.org/10.1021/jacs.2c06278
J. Am. Chem. Soc. 2022, 144, 18896−18907

was plotted vs Fe^{2+} concentration. We obtained a linear response with a correlation coefficient $R^2 = 0.99836$, Figure 5d. We observed linear behavior for the two methods at concentrations up to 4 mM, making them highly comparable. This comparison validates the performance of our method for the electrochemical detection of the $[DMPO{-}OH]^{\bullet}$ against ESR, which is regarded as the golden standard for $^{\bullet}OH$ detection.

It is also noteworthy that unlike ESR which requires strict calibration for quantitative work, electrochemical measurement of $I_{L,Tip}$ to determine the concentration of redox-active species can be easily performed using eq 4:

$$I_{L,Tip} = 4nFaDC \tag{4}$$

where n is the number of electrons transferred per redox-active molecule ($n = 1$ here), F is Faraday's constant (96 485 C mol^{-1}), a is the radius of the electrode (12.5×10^{-6} m for our UMEs), D is the diffusion coefficient of the species (here assumed to be 1×10^{-9} m^2 s^{-1}), and C is the concentration in mol/m^3. As an example from Figure 5b, when $[Fe^{2+}] = 3$ mM, the calculated concentration of $[DMPO{-}OH]^{\bullet}$ is ~0.4 mM, reflecting the instantaneous composition of the evolving Fenton solution at the time of measurement (~2 min). We hope this simpler methodology enables new studies on the chemical kinetics of $[DMPO{-}OH]^{\bullet}$ and associated reactions.

3. CONCLUSION

We introduced a versatile electroanalytical method for the detection, comparison, and imaging of $^{\bullet}OH$ at electrodes and in homogeneous solution based on the identification of the redox activity of the spin trap adduct $[DMPO{-}OH]^{\bullet}$. Reaction with DMPO allowed the $^{\bullet}OH$ radical lifetime to be extended to observe an anodic redox process at ~0.85 V vs Ag|AgCl that we unambiguously assigned to $[DMPO{-}OH]^{\bullet}$ through DFT prediction and ESR measurements. Electrochemical generation of $[DMPO{-}OH]^{\bullet}$ was estimated primarily at BDD substrates, but our method allowed probing other surfaces including PbO_2, SnO_2, GC, Pt, and Ti sheet to determine a comparative generation efficiency as a function of potential. On BDD, we determined values as high as 5% in 0.1 M Na_2SO_4 at pH 4. We also verified the homogeneity of the BDD surface reactivity using SECM imaging. Finally, we established that the electrochemical method is equally performing and linear to ESR experiments using a homogeneous Fenton chemistry for comparison.

Applications of ROS generation at electrodes for wastewater treatment, electrosynthesis, and a general understanding of interfacial electrochemical processes will likely continue to grow as electrification of the chemical toolset gathers momentum.[58−62] This makes our in situ strategy and findings timely for the characterization of a variety of known and new types electrodes. Effectively, our method dramatically simplifies the estimation and comparative analysis of $^{\bullet}OH$ by replacing the need for ESR measurements in exchange for a swift, inexpensive electrochemical collection approach. Indeed, although we decided to use SECM because of its steady-state and imaging capabilities, short time scale for species detection, and previous experience in our laboratory with methods for ROS detection,[50] there is no reason why the presented methodology cannot be deployed using other techniques such as the rotating ring-disk electrode (RRDE), provided a suitable disk electrode is available.[63] Many laboratories in countries with limited resources may not have ESR instrumentation available, but it is common to find well-established electrochemical facilities elsewhere. Thus, we hope these findings will encourage more quantitative and informed mechanistic explorations of the role of $^{\bullet}OH$ mediated oxidation processes on Fenton systems and on electrode surfaces.

4. EXPERIMENTAL SECTION

4.1. Chemicals and Solutions. 5,5-Dimethyl-1-pyrroline *N*-oxide (DMPO, 97%, Sigma-Aldrich), iron(II) chloride ($FeCl_2$, 99.5%, Sigma-Aldrich), hydrogen peroxide (H_2O_2, Macron), sodium hydroxide (NaOH, 99%, Fisher Chemicals), sodium carbonate (Na_2CO_3, 99%, Sigma-Aldrich), tripotassium phosphate tribasic (K_3PO_4, 99%, Sigma-Aldrich), potassium phosphate dibasic (K_2HPO_4, 98%, Sigma-Aldrich), potassium phosphate monobasic (KH_2PO_4, 99%, Sigma-Aldrich), sodium sulfate (Na_2SO_4, 99%, Sigma-Aldrich), sulfuric acid (H_2SO_4, 95%, Fisher chemical), and hydrochloric acid (HCl, Macron) were used as received commercially. Ultrapure water from a Millipore Synergy purifier was employed to prepare all solutions. Pb sheets (30 mm × 10 cm × 2 mm) were purchased from Goodfellow. Titanium alloys (30 mm × 10 cm × 2 mm) grade 2 (ASTM B265) were obtained from TEPSA, S. A. de C. V. FTO glasses were purchased from Millipore Sigma. The glassy carbon electrode consisted of a 1 × 1 cm^2 plate from SPI-glas 22 grade glassy carbon (SPI supplies). A Pt electrode consisted of sputtered Pt to form a 100 nm thick layer over a Si wafer. The BDD electrodes were obtained from Adamant Technologies (Switzerland) and consisted of ca. 1.2 μm thick synthetic diamond films grown on p-Si substrates. The boron doping levels were 8000 ppm, or ca. 3×10^{21} atoms per cm^3. Electrical contact was made by indium/copper tape to the backside of the silicon. We performed Raman spectroscopy characterization observing the characteristic peaks reported for BDD surfaces in Figure S13. Raman spectroscopy was performed using a Nanophoton 11 Confocal Raman Microscope. Spectra were recorded on BDD samples using a ×50 (NA 0.8) objective with a 531.94 nm and 2.15 mW power excitation laser. A grating of 600 gr/mm centered at 1500 cm^{-1} was used. Each spectrum was integrated for 5 s and averaged 5 times. The wavelengths were calibrated using a Ne lamp source. The characteristics peaks[64] for boron-doping effect at 500 and 1200 cm^{-1} in a mixture of Boron-doping effect/D Peak, sp^3 Diamond peak was detected at 1332 cm^{-1}, sp^2 Graphitic Peak was observed at 1332 cm^{-1}, and 2D Peaks were identified at 2500 cm^{-1}. Atomic force microscopy imaging of the electrode in tapping mode is shown in Figure S14. The tip used in the AFM experiments was a PPP-NCHR (k = 42 N/m, Freq = 320 Hz) from Park Instruments. The set point was 13 nm with a scan rate of 1 Hz. Five images of 25 μm × 25 μm were obtained in different areas of the sample, and their peak-to-peak roughness (Rz) values were obtained with Park XEI proprietary software and the open source software Gwyddion.[65] From these results, Rz was estimated at 657.8 ± 48.5 nm. Figure S14 shows the surface of the BDD to be highly irregular, making it difficult to measure grain sizes; however, qualitatively, we estimate that most grains are a few microns and smaller in size.

4.2. Electrode Preparation. SECM tips were fabricated by sealing gold (25 μm diameter, 99.99% purity, Goodfellow), platinum (25 μm diameter, 99.99% purity, Goodfellow), or carbon fiber wires (7 μm diameter, Goodfellow) at one end of a glass capillary. Silver epoxy was used to make connections to both gold and platinum tips, as well as conductive carbon paint thinned with isopropanol for carbon tips. The tips were sharpened with sandpaper to get an R_g about 3 and were polished with 1.0 μm alumina on polishing pads to yield a flat disk. PbO_2|Pb sheets were prepared by thermal and electrochemical oxidation following the methodology described in ref 66 employing an electro-oxidation time of 5 h. Ti sheets were polished with different grades of sandpaper ending with 0.5 μm alumina on polishing pads. Subsequently, they were washed by ultrasonic cleaning in acetone, ethanol, and deionized water for 10 min in each solvent and dried with N_2 gas.

https://doi.org/10.1021/jacs.2c06278
J. Am. Chem. Soc. 2022, 144, 18896−18907

4.3. Scanning Electrochemical Microscopy. SECM experiments were carried out using a CHI 920D scanning electrochemical microscope. UME probes of Au, C, or Pt were used as the tip working electrode, while different substrates as BDD, PbO_2|Pb, Ti sheet, or FTO glass were employed as the substrate working electrode. The substrate working electrode was held in the bottom of a Teflon cell sealed by a Viton O-ring exposing an area equal to 7.06 mm^2. The electrical connection in all substrates was made by indium/copper tape placed on the front face but isolated from solution by means of the Teflon cell. The Pt wire was used as a counter electrode, and a Ag|AgCl (3 M KCl) electrode separated from solution by a 3 M KCl|agar salt bridge was used as the reference electrode. The probes were positioned 10 μm above the substrate by negative feedback approach curves (Figure S1) using O_2 as a redox mediator. Unless otherwise indicated, all measurements were made keeping the tip at this distance.

4.4. SG/TC SECM Experimental Procedure. SG/TC experiments were carried out using 0.1 M Na_2SO_4 at pH 4 or 7, or using 0.1 M PBS at pH 7.4 solutions purged with argon gas for 10 min before and during all of the experiment to exclude O_2 from the cell. $[DMPO-OH]^\bullet$ collections were carried out using 10 mM DMPO in the electrolytic solutions. H_2O_2 collection experiments were done in the absence of DMPO. In all experiments the substrate was biased to different potentials with 60 s of quiet time. SG/TC SECM images on BDD were recorded on the $x-y$ axis with a scanning speed equal to 10 $\mu m\ s^{-1}$ to steps of 10 μm, while the BDD electrode was polarized at 1.7 V vs Ag|AgCl. A gold UME was used ($R_g = 3$) and biased to 0.9 V vs Ag|AgCl during imaging.

4.5. ESR Measurements. The spin trap 5,5-dimethyl-1-pyrroline-*N*-oxide (DMPO) was used to detect radical species. DMPO experiments at variable concentration of the spin trap were conducted at each of the solutions mentioned above. Aliquots of 150 μL were removed from electrolyzed solutions and were transferred to a Wilmad Glass quartz flat cell. The spectra samples were acquired at RT (298 K) with an EMXPlus X-band instrument. Measurement conditions: center field 3500 G, sweep field 100 G, sweep time 60 s, MW power 20 mW, gain 2.0 × 10^3, modulation amplitude 1 G, modulation frequency 100 kHz, time constant 0.064 s, MW frequency 9.50390 GHz.

4.6. Detection of Hydroxyl Radicals in Processes Based on the Fenton Reaction. Experiments with H_2O_2, Fe^{2+}, and DMPO were conducted varying the $FeCl_2$ concentration from 0 to 5 mM. Constant DMPO and H_2O_2 concentrations of 100 mM and 12.5 mM were kept constant for all experiments. For this purpose, Fenton reactions were performed by mixing reagents at the desired proportions. All solutions were prepared with 0.1 M Na_2SO_4 at pH 7. A conventional cell with a three-electrode configuration was used with a gold UME as the working electrode (25 μm diameter), Pt wire as the counter electrode, and a Ag|AgCl (3 M KCl) electrode separated from solution by a 3 M KCl|agar salt bridge as the reference electrode. Cyclic voltammograms were recorded to 10 mV s^{-1}. The same solutions were employed to get their corresponding ESR spectra.

4.7. DFT Methodology. All calculations were run using Gaussian 16.[67] Gas phase calculations were performed using the B3LYP flavor of the density functional theory (DFT), which combines exact HF exchange with the Becke generalized gradient exchange function[68] and the Lee, Yang, and Parr correlation functional (LYP).[69] The O, C, N, and H atoms were described using Pople's[70] 6-311++G** basis set, including core and valence electrons. Geometries were fully optimized for each structure. The minima were confirmed by diagonalizing the Hessian matrix and computing the vibrational frequencies. Each minimum had no imaginary frequencies. The vibrational frequencies were used to calculate zero-point energy (ZPE) and thermal corrections to QM energy at 298 K. Redox potentials in water at 298 K were predicted using two methodologies: (1) Separate computation of gas-phase free energies of formation and change in energies due to solvation (Born−Haber cycle) and (2) one-step, direct calculation of absolute redox potential by calculating thermal corrections to free energy on structures optimized with solvation.[71] The absolute redox potential (APR) of the Ox/Red couple is defined in eq 5:

$$E^\circ_{abs} = \frac{-\Delta G^\circ_{(s)}}{nF} \tag{5}$$

where $\Delta G_{(s)}{}^\circ$ is the standard Gibbs free energy change for redox event in solution (here oxidation), n is the number of electrons involved in the reaction (here $n = 1$), and F is the Faraday constant (F = 96,485 J × mol^{-1} × V^{-1} or 23.061 kcal × J × mol^{-1} × V^{-1}). The computed APR values are referenced to the standard hydrogen electrode (SHE) and subsequently referenced to the silver chloride reference electrode (Ag|AgCl). We applied two commonly used SHE reference potentials of 4.28 V[64] and 4.44 V[65] (IUPAC).[62−74] In addition to different methods for redox potential prediction, we also employed two different solvation methods to determine the optimum E° prediction: (1) Polarizable Continuum Model (PCM) using the integral equation formalism variant (IEF-PCM);[66] (2) Solvation Model based on Density (SMD).[75]

4.8. Numerical Simulations. Simulated calibration data for $[DMPO-OH]^\bullet$ collection were estimated by the finite element method using COMSOL Multiphysics v.5.2a software (COMSOL, Inc.) in axial 2D symmetry. The physics employed to resolve the simulations was the transport of diluted species module. The basics of the SG/TC simulation have been described elsewhere.[50] Figure S9a illustrates the geometries, initial values, and boundary conditions employed to perform the simulations. The simulation dimensions used were UME tip radius a = 12.5 μm with $R_g = 3$, substrate radius b = 700 μm, and distance from substrate to tip d = 10 μm (L = d/a = 0.8). This simulation represents the UME tip collection of $[DMPO-OH]^\bullet$ species which comes from substrate generation. $[DMPO-OH]^\bullet$ is the adduct formed when DMPO (C^*_{DMPO} = 10 mM), initially present in the bulk, reacts with the $^\bullet$OH radicals formed on the substrate. We used the reported $^\bullet$OH trapping rate constant by DMPO of 3.4 × 10^9 M^{-1} s^{-1}.[76,77] The SECM tip is immersed in the diffusion layer created at the substrate, and $[DMPO-OH]^\bullet$ species are oxidized to form the $[DMPO-OH]^+$ species. D_{DMPO}, D_{OH}, and $D_{DMPO-OH}$ are the diffusion coefficients for DMPO, $^\bullet$OH, and $[DMPO-OH]^\bullet$ species, which were assumed to be 1 × 10^{-9} m^2 s^{-1} according to previously estimated values.[49,78] The current density for $^\bullet$OH radicals formation on the substrate represented as flux $N_{0,OH}$ ($j_{partial} = N_{0,OH} \cdot F$, where F is the faraday constant) was changed to obtain the limiting current $I_{L,Tip}$ collected on the tip while the distance d was kept constant. Those values were used to build the calibration curve in Figure S9b.

We combined information from our simulations and from current measurements at the substrate electrode to estimate a generation efficiency for $[DMPO-OH]^\bullet$ for comparative purposes between different samples. Partial current density ($j_{partial}$) generated on the substrate for each limiting current $I_{L,Tip}$ collected on the tip was extrapolated by linear fitting in Figure S9b. The generation efficiency at each substrate and different potentials was estimated using the eq 6:

$$\text{Generation efficiency} = \frac{j_{partial}}{j_{total}} * 100 \tag{6}$$

where j_{total} is the current density measured experimentally at the substrate.

■ ASSOCIATED CONTENT

Supporting Information

The Supporting Information is available free of charge at https://pubs.acs.org/doi/10.1021/jacs.2c06278.

Approach curves, cyclic voltammetry, DFT values simulations, ESR experiments, collection experiments and COMSOL simulations. (PDF)

https://doi.org/10.1021/jacs.2c06278
J. Am. Chem. Soc. 2022, 144, 18896−18907

AUTHOR INFORMATION

Corresponding Author

Joaquín Rodríguez-López − *Department of Chemistry, University of Illinois Urbana−Champaign, Urbana, Illinois 61801, United States;* orcid.org/0000-0003-4346-4668; Email: joaquinr@illinois.edu

Authors

Jaxiry S. Barroso-Martínez − *Department of Chemistry, University of Illinois Urbana−Champaign, Urbana, Illinois 61801, United States; Centro de Investigación y Desarrollo Tecnológico en Electroquímica, S.C. Parque Tecnológico Querétaro, Sanfandila, Pedro Escobedo 76703 Querétaro, Mexico;* orcid.org/0000-0003-4059-5021

Adolfo I. B. Romo − *Department of Chemistry, University of Illinois Urbana−Champaign, Urbana, Illinois 61801, United States;* orcid.org/0000-0002-9288-2420

Sanja Pudar − *Department of Chemistry, University of Illinois Urbana−Champaign, Urbana, Illinois 61801, United States*

Seth T. Putnam − *Department of Chemistry, University of Illinois Urbana−Champaign, Urbana, Illinois 61801, United States*

Erika Bustos − *Centro de Investigación y Desarrollo Tecnológico en Electroquímica, S.C. Parque Tecnológico Querétaro, Sanfandila, Pedro Escobedo 76703 Querétaro, Mexico*

Complete contact information is available at: https://pubs.acs.org/10.1021/jacs.2c06278

Author Contributions

§J.S.B.-M. and A.I.B.R. have equal contribution in this work.

Notes

The authors declare no competing financial interest.

ACKNOWLEDGMENTS

This material is based upon work supported by the National Science Foundation under CHE Grant 2004054. We appreciate the assistance of Dr. Oliver Rodríguez Martínez in obtaining the AFM measurements. Additionally, portions of this work were carried out in part in the Materials Research Laboratory Central Research Facilities, University of Illinois.

REFERENCES

(1) Proctor, A. D.; Bartlett, B. M. Hydroxyl Radical Suppression during Photoelectrocatalytic Water Oxidation on WO_3|FeOOH. *J. Phys. Chem. C* **2020**, *124* (33), 17957−17963.

(2) Siahrostami, S.; Li, G.-L.; Viswanathan, V.; Nørskov, J. K. One- or Two-Electron Water Oxidation, Hydroxyl Radical, or H_2O_2 Evolution. *J. Phys. Chem. Lett.* **2017**, *8* (6), 1157−1160.

(3) Wang, L.; Li, B.; Dionysiou, D. D.; Chen, B.; Yang, J.; Li, J. Overlooked Formation of H_2O_2 during the Hydroxyl Radical-Scavenging Process When Using Alcohols as Scavengers. *Environ. Sci. Technol.* **2022**, *56* (6), 3386−3396.

(4) Hashmi, M. Z.; Kaleem, M.; Farooq, U.; Su, X.; Chakraborty, P.; Rehman, S. U. Chemical remediation and advanced oxidation process of polychlorinated biphenyls in contaminated soils: a review. *Environmental Science and Pollution Research* **2022**, *29* (16), 22930−22945.

(5) Lutic, D.; Sescu, A. M.; Siamer, S.; Harja, M.; Favier, L. Excellent ambient oxidation and mineralization of an emerging water pollutant using Pd-doped TiO_2 photocatalyst and UV-A irradiation. *J. Comptes Rendus Chimie.* **2022**, 1−13.

(6) Prado, C. A.; Antunes, F. A. F.; Rocha, T. M.; Sánchez-Muñoz, S.; Barbosa, F. G.; Terán-Hilares, R.; Cruz-Santos, M. M.; Arruda, G. L.; da Silva, S. S.; Santos, J. C. A review on recent developments in hydrodynamic cavitation and advanced oxidative processes for pretreatment of lignocellulosic materials. *Bioresour. Technol.* **2022**, *345*, 126458.

(7) Wang, Z.; Qiu, W.; Pang, S.-y.; Guo, Q.; Guan, C.; Jiang, J. Aqueous Iron(IV)−Oxo Complex: An Emerging Powerful Reactive Oxidant Formed by Iron(II)-Based Advanced Oxidation Processes for Oxidative Water Treatment. *Environ. Sci. Technol.* **2022**, *56* (3), 1492−1509.

(8) Domingues, E.; Fernandes, E.; Gomes, J.; Martins, R. C. Advanced oxidation processes perspective regarding swine wastewater treatment. *Science of The Total Environment* **2021**, *776*, 145958.

(9) Ganiyu, S. O.; Martínez-Huitle, C. A.; Oturan, M. A. Electrochemical advanced oxidation processes for wastewater treatment: Advances in formation and detection of reactive species and mechanisms. *Current Opinion in Electrochemistry* **2021**, *27*, 100678.

(10) Ji, R.; Chen, J.; Liu, T.; Zhou, X.; Zhang, Y. Critical review of perovskites-based advanced oxidation processes for wastewater treatment: Operational parameters, reaction mechanisms, and prospects. *Chin. Chem. Lett.* **2022**, *33* (2), 643−652.

(11) Kusumoto, T.; Ogawara, R.; Igawa, K.; Baba, K.; Konishi, T.; Furusawa, Y.; Kodaira, S. Scaling parameter of the lethal effect of mammalian cells based on radiation-induced OH radicals: effectiveness of direct action in radiation therapy. *Journal of Radiation Research* **2021**, *62* (1), 86−93.

(12) Li, X.; Wu, D.; Hua, T.; Lan, X.; Han, S.; Cheng, J.; Du, K.-S.; Hu, Y.; Chen, Y. Micro/macrostructure and multicomponent design of catalysts by MOF-derived strategy: Opportunities for the application of nanomaterials-based advanced oxidation processes in wastewater treatment. *Science of The Total Environment* **2022**, *804*, 150096.

(13) Liu, L.; Chen, Z.; Zhang, J.; Shan, D.; Wu, Y.; Bai, L.; Wang, B. Treatment of industrial dye wastewater and pharmaceutical residue wastewater by advanced oxidation processes and its combination with nanocatalysts: A review. *Journal of Water Process Engineering* **2021**, *42*, 102122.

(14) Mahtab, M. S.; Farooqi, I. H.; Khursheed, A. Zero Fenton sludge discharge: a review on reuse approach during wastewater treatment by the advanced oxidation process. *International Journal of Environmental Science and Technology* **2022**, *19* (3), 2265−2278.

(15) Mousset, E.; Loh, W. H.; Lim, W. S.; Jarry, L.; Wang, Z.; Lefebvre, O. Cost comparison of advanced oxidation processes for wastewater treatment using accumulated oxygen-equivalent criteria. *Water Res.* **2021**, *200*, 117234.

(16) Rayaroth, M. P.; Aravindakumar, C. T.; Shah, N. S.; Boczkaj, G. Advanced oxidation processes (AOPs) based wastewater treatment - unexpected nitration side reactions - a serious environmental issue: A review. *Chemical Engineering Journal* **2022**, *430*, 133002.

(17) Tanaka, H.; Mizuno, M.; Ishikawa, K.; Toyokuni, S.; Kajiyama, H.; Kikkawa, F.; Hori, M. Cancer Treatments Using Low-Temperature Plasma. *Curr. Med. Chem.* **2021**, *28* (41), 8549−8558.

(18) Xia, H.; Li, C.; Yang, G.; Shi, Z.; Jin, C.; He, W.; Xu, J.; Li, G. A review of microwave-assisted advanced oxidation processes for wastewater treatment. *Chemosphere* **2022**, *287*, 131981.

(19) Jafari, B.; Godini, H.; Soltani, R. D. C.; Seydi, E. Effectiveness of UV/SO_3^{2-} advanced reduction process for degradation and mineralization of trichlorfon pesticide in water: identification of intermediates and toxicity assessment. *Environmental Science and Pollution Research* **2022**, *29* (14), 20409−20420.

(20) Lu, Z.; Xu, Y.; Peng, L.; Liang, C.; Liu, Y.; Ni, B.-J. A two-stage degradation coupling photocatalysis to microalgae enhances the mineralization of enrofloxacin. *Chemosphere* **2022**, *293*, 133523.

(21) Sinha, S.; Roy, D.; Roy, O.; Neogi, S.; De, S. Removal of organic contaminants from flowback water using Fenton process. *Journal of Water Process Engineering* **2022**, *47*, 102680.

(22) Xu, J.; Sun, M.; Zhang, C.; Wu, M.; Fu, D. Electrochemical mineralization of direct blue 71 with boron-doped diamond anodes: Factor analysis and mechanisms study. *Journal of Environmental Chemical Engineering* **2022**, *10* (1), 107031.

(23) Marselli, B.; Garcia-Gomez, J.; Michaud, P. A.; Rodrigo, M. A.; Comninellis, C. Electrogeneration of Hydroxyl Radicals on Boron-Doped Diamond Electrodes. *J. Electrochem. Soc.* **2003**, *150* (3), D79.
(24) Panizza, M.Importance of Electrode Material in the Electrochemical Treatment of Wastewater Containing Organic Pollutants. In *Electrochemistry for the Environment*; Comninellis, C., Chen, G., Eds.; Springer New York: New York, NY, 2010; pp 25−54.
(25) Sun, S.; Yao, H.; Fu, W.; Liu, F.; Wang, X.; Zhang, W. Enhanced degradation of carbamazepine in FeOCl based Photo-Fenton reaction. *Journal of Environmental Chemical Engineering* **2021**, *9* (1), 104501.
(26) Yang, Y.; Wang, Q.; Aleisa, R.; Zhao, T.; Ma, S.; Zhang, G.; Yao, T.; Yin, Y. MoS_2/FeS Nanocomposite Catalyst for Efficient Fenton Reaction. *ACS Appl. Mater. Interfaces* **2021**, *13* (44), 51829−51838.
(27) Divyapriya, G.; Singh, S.; Martínez-Huitle, C. A.; Scaria, J.; Karim, A. V.; Nidheesh, P. V. Treatment of real wastewater by photoelectrochemical methods: An overview. *Chemosphere* **2021**, *276*, 130188.
(28) Hwang, J. Y.; Moon, G.-h.; Kim, B.; Tachikawa, T.; Majima, T.; Hong, S.; Cho, K.; Kim, W.; Choi, W. Crystal phase-dependent generation of mobile OH radicals on TiO2: Revisiting the photocatalytic oxidation mechanism of anatase and rutile. *Applied Catalysis B: Environmental* **2021**, *286*, 119905.
(29) Treviño-Reséndez, J.; Medel, A.; Mijaylova, P.; Robles, I.; Rodríguez-Valadez, F.; Godínez, L. A.; Meas, Y. Insight into the generation of hydroxyl radicals by photo-electrocoagulation process via active chlorine. *International Journal of Environmental Science and Technology* **2022**, *19* (4), 2913−2924.
(30) Cornejo, O. M.; Murrieta, M. F.; Castañeda, L. F.; Nava, J. L. Electrochemical reactors equipped with BDD electrodes: Geometrical aspects and applications in water treatment. *Curr. Opin. Solid State Mater. Sci.* **2021**, *25* (4), 100935.
(31) Mbaye, M.; Diaw, P. A.; Mbaye, O. M. A.; Oturan, N.; Gaye Seye, M. D.; Trellu, C.; Coly, A.; Tine, A.; Aaron, J. J.; Oturan, M. A. Rapid removal of fungicide thiram in aqueous medium by electro-Fenton process with Pt and BDD anodes. *Sep. Purif. Technol.* **2022**, *281*, 119837.
(32) Oturan, M. A. Outstanding performances of the BDD film anode in electro-Fenton process: Applications and comparative performance. *Curr. Opin. Solid State Mater. Sci.* **2021**, *25* (3), 100925.
(33) Sandoval, M. A.; Calzadilla, W.; Salazar, R. Influence of reactor design on the electrochemical oxidation and disinfection of wastewaters using boron-doped diamond electrodes. *Current Opinion in Electrochemistry* **2022**, *33*, 100939.
(34) Macpherson, J. V. A practical guide to using boron doped diamond in electrochemical research. *Phys. Chem. Chem. Phys.* **2015**, *94* (27), 9856−9862.
(35) Dong, H.; Hu, X.; Zhang, Y.; Jiang, W.; Zhang, X. Co/La modified Ti/PbO_2 anodes for chloramphenicol degradation: Catalytic performance and reaction mechanism. *Chemosphere* **2021**, *285*, 131568.
(36) Wang, H.; Li, Z.; Zhang, F.; Wang, Y.; Zhang, X.; Wang, J.; He, X. Comparison of Ti/Ti_4O_7, Ti/Ti_4O_7-PbO_2-Ce, and Ti/Ti_4O_7 nanotube array anodes for electro-oxidation of p-nitrophenol and real wastewater. *Sep. Purif. Technol.* **2021**, *266*, 118600.
(37) Zhu, X.; Hu, W.; Feng, C.; Chen, N.; Chen, H.; Kuang, P.; Deng, Y.; Ma, L. Electrochemical oxidation of aniline using Ti/RuO_2-SnO_2 and Ti/RuO_2-IrO_2 as anode. *Chemosphere* **2021**, *269*, 128734.
(38) SIES, H. Strategies of antioxidant defense. *European Journal of Biochesmitry* **1993**, *215* (2), 213−219.
(39) Levín, P.; Ruiz, M. C.; Romo, A. I. B.; Nascimento, O. R.; Di Virgilio, A. L.; Oliver, A. G.; Ayala, A. P.; Diógenes, I. C. N.; León, I. E.; Lemus, L. Water-mediated reduction of $[Cu(dmp)_2(CH_3CN)]^{2+}$: implications of the structure of a classical complex on its activity as an anticancer drug. *Inorganic Chemistry Frontiers* **2021**, *8* (13), 3238−3252.
(40) Romo, A. I. B.; Carepo, M. P.; Levín, P.; Nascimento, O. R.; Díaz, D. E.; Rodríguez-López, J.; León, I. E.; Bezerra, L. F.; Lemus, L.; Diógenes, I. C. N. Synergy of DNA intercalation and catalytic activity of a copper complex towards improved polymerase inhibition and cancer cell cytotoxicity. *Dalton Transactions* **2021**, *50* (34), 11931−11940.
(41) Romo, A. I. B.; Dibo, V. S.; Abreu, D. S.; Carepo, M. S. P.; Neira, A. C.; Castillo, I.; Lemus, L.; Nascimento, O. R.; Bernhardt, P. V.; Sousa, E. H. S.; Diógenes, I. C. N. Ascorbyl and hydroxyl radical generation mediated by a copper complex adsorbed on gold. *Dalton Transactions* **2019**, *48* (37), 14128−14137.
(42) Buettner, G. R. The spin trapping of superoxide and hydroxyl free radicals with DMPO (5,5-dimethylpyrroline-N-oxide): more about iron. *Free radical research communications* **1993**, *19* (sup1), S79−S87.
(43) Bilski, P.; Reszka, K.; Bilska, M.; Chignell, C. F. Oxidation of the Spin Trap 5,5-Dimethyl-1-pyrroline N-Oxide by Singlet Oxygen in Aqueous Solution. *J. Am. Chem. Soc.* **1996**, *118* (6), 1330−1338.
(44) Fontmorin, J. M.; Burgos Castillo, R. C.; Tang, W. Z.; Sillanpää, M. Stability of 5,5-dimethyl-1-pyrroline-N-oxide as a spin-trap for quantification of hydroxyl radicals in processes based on Fenton reaction. *Water Res.* **2016**, *99*, 24−32.
(45) Braxton, E.; Fox, D.; Breeze, B.; Tully, J.; Levey, K.; Newton, M.; Macpherson, J.Electron Paramagnetic Resonance for the Detection of Electrochemically Generated Hydroxyl Radicals: Issues Associated with Electrochemical Oxidation of the Spin Trap. *ChemRxiv*. DOI: 10.26434/chemrxiv-2022-mxq0n (accessed 2022-07-15).
(46) Myers, B.; Ranieri, P.; Smirnova, T.; Hewitt, P.; Peterson, D.; Herrera Quesada, M.; Lenker, E.; Stapelmann, K. Measuring plasma-generated •OH and O atoms in liquid using EPR spectroscopy and the non-selectivity of the HTA assay. *J. Phys. D: Appl. Phys.* **2021**, *54* (14), 145202.
(47) Chen, C.; Li, F.; Chen, H. L.; Kong, M. G. Interaction between air plasma-produced aqueous $^1O_2$ and the spin trap DMPO in electron spin resonance. *Physics of plasmas* **2017**, *24* (10), 103501.
(48) Sánchez-Sánchez, C. M.; Rodríguez-López, J.; Bard, A. J. Scanning Electrochemical Microscopy. 60. Quantitative Calibration of the SECM Substrate Generation/Tip Collection Mode and Its Use for the Study of the Oxygen Reduction Mechanism. *Anal. Chem.* **2008**, *80* (9), 3254−3260.
(49) Pei, S.; You, S.; Ma, J.; Chen, X.; Ren, N. Electron Spin Resonance Evidence for Electro-generated Hydroxyl Radicals. *Environ. Sci. Technol.* **2020**, *54* (20), 13333−13343.
(50) Counihan, M. J.; Setwipatanachai, W.; Rodríguez-López, J. Interrogating the Surface Intermediates and Water Oxidation Products of Boron-Doped Diamond Electrodes with Scanning Electrochemical Microscopy. *ChemElectroChem.* **2019**, *6* (13), 3507−3515.
(51) Bard, A. J. Inner-Sphere Heterogeneous Electrode Reactions. Electrocatalysis and Photocatalysis: The Challenge. *J. Am. Chem. Soc.* **2010**, *132* (22), 7559−7567.
(52) Comninellis, C.; Gohua, C.*Electrochemistry for the Environment*; Springer: 2010.
(53) Cuerda-Correa, E. M.; Alexandre-Franco, M. F.; Fernández-González, C. Advanced Oxidation Processes for the Removal of Antibiotics from Water. An Overview. *Water* **2020**, *12* (1), 102.
(54) Henke, A. H.; Saunders, T. P.; Pedersen, J. A.; Hamers, R. J. Enhancing Electrochemical Efficiency of Hydroxyl Radical Formation on Diamond Electrodes by Functionalization with Hydrophobic Monolayers. *Langmuir* **2019**, *35* (6), 2153−2163.
(55) Marković, N. M.; Ross, P. N. Surface science studies of model fuel cell electrocatalysts. *Surf. Sci. Rep.* **2002**, *45*, 117−229.
(56) Quaino, P.; Schmickler, W. Oxygen-Terminated Diamond Electrodes in Alkaline Media: Structure and OH Generation. *ChemElectrochem* **2014**, *1*, 933−939.
(57) Kapalka, A.; Foti, G.; Comninellis, C. The importance of electrode material in environmental electrochemistry: Formation and reactivity of free hydroxyl radicals on boron-doped diamond electrodes. *Electrochim. Acta* **2009**, *54*, 2018−2023.

(58) Dey, A.; Gunnoe, T. B.; Stamenkovic, V. R. Organic Electrosynthesis: When Is It Electrocatalysis? *ACS Catal.* **2020**, *10* (21), 13156−13158.
(59) Malapit, C. A.; Prater, M. B.; Cabrera-Pardo, J. R.; Li, M.; Pham, T. D.; McFadden, T. P.; Blank, S.; Minteer, S. D. Advances on the Merger of Electrochemistry and Transition Metal Catalysis for Organic Synthesis. *Chem. Rev.* **2022**, *122* (3), 3180−3218.
(60) Minteer, S. D.; Baran, P. Electrifying Synthesis: Recent Advances in the Methods, Materials, and Techniques for Organic *Electrosynthesis*. *Acc. Chem. Res.* **2020**, *53* (3), 545−546.
(61) Rodrigo, S.; Gunasekera, D.; Mahajan, J. P.; Luo, L. Alternating current electrolysis for organic synthesis. *Current Opinion in Electrochemistry* **2021**, *28*, 100712.
(62) Shatskiy, A.; Lundberg, H.; Kärkäs, M. D. Organic Electrosynthesis: Applications in Complex Molecule Synthesis. *Chem. Electro. Chem.* **2019**, *6* (16), 4067−4092.
(63) Tully, J. J.; Zhang, Z.; Rodríguez, I. M.; Butcher, L.; Macpherson, J. V. Versatile DIY Route for Incorporation of a Wide Range of Electrode Materials into Rotating Ring Disk Electrodes. *Anal. Chem.* **2022**, *94* (27), 9856−9862.
(64) Dec, B.; Ficek, M.; Rycewicz, M.; Macewicz, L.; Gnyba, m.; Sawczak, M.; Sobaszek, M.; Bogdanowicz, R. Gas composition influence on the properties of boron-doped diamond films deposited on the fused silica. *Materials Science-Poland* **2018**, *36*, 288−296.
(65) Nečas, D.; Klapetek, P. Gwyddion: an open-source software for SPM data analysis. *Central European Journal of Physics* **2012**, *10*, 181−188.
(66) Chen, Z.; Xie, G.; Pan, Z.; Zhou, X.; Lai, W.; Zheng, L.; Xu, Y. A novel Pb/PbO_2 electrodes prepared by the method of thermal oxidation-electrochemical oxidation: Characteristic and electrocatalytic oxidation performance. *J. Alloys Compd.* **2021**, *851*, 156834.
(67) Frisch, M. J.; Trucks, G. W.; Schlegel, H. B.; Scuseria, G. E.; Robb, M. A.; Cheeseman, J. R.; Scalmani, G.; Barone, V.; Petersson, G. A.; Nakatsuji, H.; Li, X.; Caricato, M.; Marenich, A. V.; Bloino, J.; Janesko, B. G.; Gomperts, R.; Mennucci, B.; Hratchian, H. P.; Ortiz, J. V.; Izmaylov, A. F.; Sonnenberg, J. L.; Williams; Ding, F.; Lipparini, F.; Egidi, F.; Goings, J.; Peng, B.; Petrone, A.; Henderson, T.; Ranasinghe, D.; Zakrzewski, V. G.; Gao, J.; Rega, N.; Zheng, G.; Liang, W.; Hada, M.; Ehara, M.; Toyota, K.; Fukuda, R.; Hasegawa, J.; Ishida, M.; Nakajima, T.; Honda, Y.; Kitao, O.; Nakai, H.; Vreven, T.; Throssell, K.; Montgomery, J. A., Jr.; Peralta, J. E.; Ogliaro, F.; Bearpark, M. J.; Heyd, J. J.; Brothers, E. N.; Kudin, K. N.; Staroverov, V. N.; Keith, T. A.; Kobayashi, R.; Normand, J.; Raghavachari, K.; Rendell, A. P.; Burant, J. C.; Iyengar, S. S.; Tomasi, J.; Cossi, M.; Millam, J. M.; Klene, M.; Adamo, C.; Cammi, R.; Ochterski, J. W.; Martin, R. L.; Morokuma, K.; Farkas, O.; Foresman, J. B.; Fox, D. J.*Gaussian 16*, Rev. C.01; Gaussian Inc.: Wallingford, CT, 2016.
(68) Becke, A. D. Density-functional exchange-energy approximation with correct asymptotic behavior. *Phys. Rev. A* **1988**, *38* (6), 3098−3100.
(69) Lee, C.; Yang, W.; Parr, R. G. Development of the Colle-Salvetti correlation-energy formula into a functional of the electron density. *Phys. Rev. B* **1988**, *37* (2), 785−789.
(70) Hehre, W. J. R. L.; Schleyer, P. v. R.; Pople, J. A.*Ab Initio Molecular Orbital Theory*; Wiley: New York, 1986; pp 189−295.
(71) Davis, A. P.; Fry, A. J. Experimental and Computed Absolute Redox Potentials of Polycyclic Aromatic Hydrocarbons are Highly Linearly Correlated Over a Wide Range of Structures and Potentials. *J. Phys. Chem. A* **2010**, *114* (46), 12299−12304.
(72) Yan, L.; Lu, Y.; Li, X. A density functional theory protocol for the calculation of redox potentials of copper complexes. *Phys. Chem. Chem. Phys.* **2016**, *18* (7), 5529−5536.
(73) Trasatti, S. The absolute electrode potential: an explanatory note (Recommendations 1986). *J. Pure and Applied Chemistry* **1986**, *58* (7), 955−966.
(74) Tomasi, J.; Mennucci, B.; Cammi, R. Quantum Mechanical Continuum Solvation Models. *Chem. Rev.* **2005**, *105* (8), 2999−3094.
(75) Marenich, A. V.; Cramer, C. J.; Truhlar, D. G. Universal Solvation Model Based on Solute Electron Density and on a Continuum Model of the Solvent Defined by the Bulk Dielectric Constant and Atomic Surface Tensions. *J. Phys. Chem. B* **2009**, *113* (18), 6378−6396.
(76) Gligorovski, S.; Strekowski, R.; Barbati, S.; Vione, D. Environmental Implications of Hydroxyl Radicals ($^{\bullet}OH$). *Chem. Rev.* **2015**, *115* (24), 13051−13092.
(77) Kishimoto, N.; Minakata, D.; Somiya, I. Effects of Hydrodynamic Conditions on $^{\bullet}OH$ Radical Production at Ti/Pt Anodes During Electrochemical Treatment. *Environmental Technology* **2005**, *26* (10), 1161−1172.
(78) Campo, M. G.; Grigera, J. R. Classical molecular-dynamics simulation of the hydroxyl radical in water. *J. Chem. Phys.* **2005**, *123* (8), 084507.

https://doi.org/10.1021/jacs.2c06278
J. Am. Chem. Soc. 2022, 144, 18896−18907